Monthly Notices of the ROYAL ASTRONOMICAL SOCIETY

MNRAS **534,** L42–L47 (2024) https://doi.org/10.1093/mnrasl/slae079
Advance Access publication 2024 August 21

Counter-rotation and slow precession in aligned eccentric nuclear discs due to gravitational wave recoil kicks

Jane C. Bright [1,2★] Tatsuya Akiba[2] and Ann-Marie Madigan[2]

[1]*Department of Astronomy and Steward Observatory, University of Arizona, Tucson, AZ 85719, USA*
[2]*JILA and Department of Astrophysical and Planetary Sciences, University of Colorado, Boulder, CO 80309, USA*

Accepted 2024 August 19. Received 2024 August 1; in original form 2024 June 20

ABSTRACT

The M31 nucleus contains a supermassive black hole embedded in a massive stellar disc of apsidally aligned eccentric orbits. It has recently been shown that this disc is slowly precessing at a rate consistent with zero. Here, we demonstrate using *N*-body methods that apsidally aligned eccentric discs can form with a significant (∼0.5) fraction of orbits counter-rotating as the result of a gravitational wave recoil kick of merging supermassive black holes. Higher amplitude kicks map to a larger retrograde fraction in the surrounding stellar population, which in turn results in slow precession. We furthermore show that discs with significant counter-rotation are more stable (i.e. apsidal alignment is most pronounced and long lasting), more eccentric, and have the highest rates of stars entering the black hole's tidal disruption radius.

Key words: stars: kinematics and dynamics – galaxies: kinematics and dynamics – galaxies: nuclei – transients: tidal disruption events.

1 INTRODUCTION

The nucleus of the Andromeda galaxy (M31) contains a double-peaked stellar light profile, well explained by an apsidally aligned, eccentric stellar disc in orbit about a supermassive black hole (Light, Danielson & Schwarzschild 1974; Lauer et al. 1993, 1998; Tremaine 1995; Kormendy & Bender 1999; Statler et al. 1999; Bacon et al. 2001; Sambhus & Sridhar 2002; Peiris & Tremaine 2003; Bender et al. 2005). While differential apsidal precession between orbits of varying angular momentum and energy should destabilize such discs, inter-orbit gravitational torques (Rauch & Tremaine 1996) act to maintain the apsidal alignment (Madigan et al. 2018). One might expect the disc to precess at a rate of $\sim(M_{\rm disc}/M_\bullet)\,P^{-1}$, where $M_{\rm disc}$ is the mass of the disc, $M_\bullet$ is the black hole mass, and P is the orbital period of a typical star. For $M_\bullet/M_{\rm disc} \approx \mathcal{O}(10)$ (corresponding to $M_\bullet = 10^8\ {\rm M}_\odot$ as in M31) (Bender et al. 2005; McConnachie et al. 2005), this yields a rate of $\sim$65 km s^{-1} pc^{-1}. A wide range of precession values, from 3 to 34 km s^{-1} pc^{-1}, have been found in simulations of the M31 nuclear disc using a variety of techniques (Bacon et al. 2001; Jacobs & Sellwood 2001; Salow & Statler 2001, 2004; Sambhus & Sridhar 2002). However, Lockhart et al. (2018) have shown that the lopsided disc in the Andromeda nucleus has a precession rate consistent with zero: 0 ± 3.9 km s^{-1} pc^{-1}. This rate is in agreement with the formation mechanism for the young circular disc of stars in the M31 nucleus as put forward in Chang et al. (2007) (see also Brown et al. 1998; Lauer et al. 1998, 2012; Bender et al. 2005). In Chang's scenario, mass-loss from giant stars and subsequent collisions between crossing gas streams lead to fresh star formation in a disc around the supermassive black hole every 500 Myr. The crossing orbits rely on a small precession rate ($\lesssim$3–10 km s^{-1} pc^{-1}) for the eccentric disc.

Counter-rotation has been shown to be a critical dynamical driver of lopsided Kepler discs and has a significant impact on the precession rate (Touma 2002; Touma, Tremaine & Kazandjian 2009; Sridhar & Saini 2010; Touma & Sridhar 2012; Kazandjian & Touma 2013; Touma & Tremaine 2014). Kazandjian & Touma (2013) found that discs with a counter-rotating population with one-tenth the mass produce a disc that precesses at a near-constant rate of $\sim$ 4 km s^{-1} pc^{-1}. Sridhar & Saini (2010) demonstrated no net rotation in the case of counter-rotating populations with identical radial profiles and masses, which was then recovered by Touma & Tremaine (2014) in their studies of maximum entropy equilibria for self-gravitating near-Keplerian discs. The primary proposed mechanism in these studies for explaining the presence of a counter-rotating population of stars is accretion of a globular cluster that spirals into the galactic nucleus due to dynamical friction on to a pre-existing disc of stars around the black hole (Sambhus & Sridhar 2002). Alternatively, Hopkins & Quataert (2010) showed that eccentric nuclear discs may instead originate in gas-rich galaxy mergers. This occurs when gas that is funnelled to the centre of the potential fragments and forms stars on aligned eccentric orbits, which can result in slow precession rates of 1–5 km s^{-1} pc^{-1} (see also Generozov, Nayakshin & Madigan 2022). Both the above scenarios involve external accretion into the nucleus to produce counter-rotation.

Akiba & Madigan (2021) showed that gravitational wave (GW) recoil kicks of merging black holes can reshape the surrounding stellar population into an apsidally aligned eccentric disc. Akiba & Madigan (2023) noted that stars at large distances from the black hole can reverse orbital orientation post-kick. They showed that counter-rotating populations will not have identical radial profiles even in

★ E-mail: janebright@arizona.edu

regions of the disc that have equal masses in each. The previous study used massless stellar particles and did not explore the long-term evolution of such discs. In this letter, we evolve simple post-kick stellar systems in time including the self-gravity of the stars to explore the evolution of aligned eccentric disc of stars with varying fractions of counter-rotation.

In Section 2, we describe how GW recoil kicks induce counter-rotation. In Section 3, we describe the set-up of our *N*-body simulations. In Section 4, we present our results, specifically exploring disc alignment, eccentricity evolution, precession rate, and the tidal disruption event (TDE) rate of eccentric nuclear discs produced after a black hole merger GW recoil kick. We show that significant counter-rotation induced by GW recoil kicks elevates all of these measures. We critically discuss our results in Section 5.

2 GRAVITATIONAL WAVE RECOIL KICKS

High-amplitude GWs are emitted during the final stages of binary black hole inspiral and merger. Where there is asymmetry in the binary system (arising from unequal masses and/or spins), the emission is anisotropic, resulting in a GW recoil kick imparted on the remnant black hole (Peres 1962; Bekenstein 1973; Wiseman 1992; Campanelli et al. 2007; Herrmann et al. 2007).

In Akiba & Madigan (2021, 2023), we investigated the effects of GW recoil kicks on orbiting stars. Here, we expand on the case of an initially circular disc of stars and an in-plane recoil kick. A circular stellar disc may form from a self-gravitating accretion disc (Paczynski 1978; Goodman 2003). The merger of two supermassive black holes leaves behind a flattened ellipsoid that is tangentially anisotropic in the inner regions (Mastrobuono-Battisti et al. 2023), for which a circular disc is a reasonable first-order approximation. The in-plane kick produces an apsidally aligned eccentric disc, with the net eccentricity vector orthogonal to the kick direction in the $+y$ direction. The orbital motion of bound stars in the rest frame of the kicked black hole depends on which radial regime it initially lies in: (1) where $v_{\rm circ} > v_{\rm kick}$, all stars become eccentric and remain on prograde orbits; (2) where $v_{\rm circ} < v_{\rm kick}$, orbits may become retrograde depending on their pre-kick anomaly; and (3) where $2v_{\rm circ} < v_{\rm kick}$, retrograde orbits may become anti-aligned, i.e. their net eccentricity vectors point in the $-y$ direction. All bound orbits become retrograde in the frame of the moving black hole where $v_{\rm circ} \leq \frac{1}{\sqrt{3}}\, v_{\rm kick}$. As $v_{\rm kick}$ increases, the semimajor axis range in which stars become retrograde post-kick moves inwards, causing a larger total fraction of orbits to counter-rotate.

3 *N*-BODY SIMULATIONS

3.1 Methods

We use the `IAS15` integrator in the *N*-body simulation package REBOUND (Rein & Liu 2012; Rein & Spiegel 2015). We use code units of $G = 1$, $M_\bullet = 1$, and the inner edge of the disc $a_{\rm in} = 1$ such that the period of a circular orbit at the inner edge of the disc is $P(a_{\rm in}) = 2\pi$. We initialize a circular stellar disc of stars in a semimajor axis range of $a_{\rm in} = 0.01$ and $a_{\rm out} = 4$ with a surface density profile drawn from $\Sigma \sim a^{-1}$. Inclinations are normally distributed with a standard deviation of 0.05 rad. We assume a recoil kick in the plane of the stellar disc as motivated by Bogdanović, Reynolds & Miller (2007), suggesting that the alignment of orbits and black hole spins would skew the distribution towards more in-plane kicks. Since the pre-kick disc is axisymmetric, we impart the kick in the $+x$ direction without loss of generality. For consistency of comparison across our four models, we vary the number of stars in the initial disc between $N = 10^3$ and 10^5 such that post-kick there remain $N \sim 200$ bound stars with post-kick orbits within a semimajor axis range of $a \in [1, 2]$ in code units with a disc mass of $M_{\rm disc} = 10^{-2} M_\bullet$. We then select only the stars in this range to evolve in our simulations so that we can make comparisons between our models of analogous segments of the disc and limit the computational expense of our simulations. As we are restricted in the number of *N*-body particles, each particle is overmassive compared to reality. As the ratio of the two-body relaxation time-scale to the secular (orbit-averaged) time-scale scales inversely with stellar mass, we expect our simulations to exhibit overly strong two-body scattering that perturbs particles off their orbits and weakens orbit-averaged torques. Post-Newtonian effects are excluded from these simulations since the precession time-scale due to secular torques is several orders of magnitude shorter than the estimated general relativistic precession time-scale (Naoz 2016). The dynamics and corresponding tidal disruption rates in eccentric discs are unaffected by the inclusion of post-Newtonian terms (Wernke & Madigan 2019).

The magnitude of the GW recoil kick plays an important role in the post-kick retrograde fraction. We perform four different sets of simulations (five realizations each) varying the kick magnitude to produce post-kick stellar configurations with 0 per cent retrograde (i.e. all prograde), 25 per cent retrograde, 50 per cent retrograde, and 75 per cent retrograde orbits. Simulations are labelled r_0, r_{25}, r_{50}, and r_{75}, respectively. The corresponding kick magnitudes in code units are $v_{\rm kick} = 0.5, 0.64, 0.82,$ and 1.83. The initial, post-kick, orbital configurations can be seen in the top panel of Fig. 1. The bottom panel shows the corresponding initial z-component of the orbital angular momentum normalized by the circular angular momentum, $j_z/j_{\rm circ}$, for each star. $j_z/j_{\rm circ} > 0$ are prograde orbits and $j_z/j_{\rm circ} < 0$ are retrograde. The r_{50} simulations have a very small positive net angular momentum, $j_z/j_{\rm circ} > 0$. Unless otherwise specified, we scale the mass of the black hole to $M_\bullet = 10^8\ {\rm M}_\odot$, and the inner edge of the disc to 1 pc, when calculating physical time-scales, loosely modelled on the M31 nucleus. Kick magnitudes in this case map to $v_{\rm kick} = 328, 420, 538,$ and 1200 km s^{-1}. Typical kick velocities due to anisotropic GWs are $\mathcal{O}(100\ {\rm km\ s^{-1}})$, but can reach several thousand kilometres per second (Favata, Hughes & Holz 2004; Blanchet, Qusailah & Will 2005; Damour & Gopakumar 2006; Campanelli et al. 2007).

4 RESULTS

4.1 Oscillations in stellar angular momentum

Orbit orientation is given by the eccentricity vector

$$\boldsymbol{e} = \frac{\boldsymbol{v} \times \boldsymbol{j}}{GM_\bullet} - \frac{\boldsymbol{r}}{r}, \tag{1}$$

where $\boldsymbol{r}$ is the radius vector, $\boldsymbol{v}$ is the velocity vector, $|\boldsymbol{j}| = |\boldsymbol{r} \times \boldsymbol{v}| = [GM_\bullet a(1-e^2)]^{1/2}$ is the specific angular momentum vector, a is the semimajor axis, e is the eccentricity, and $M_\bullet$ is the mass of the central black hole. The precession of an orbit is defined by the rate of change of the eccentricity vector

$$\boldsymbol{e}' = \frac{\boldsymbol{f} \times \boldsymbol{j}}{GM_\bullet} + \frac{\boldsymbol{v} \times \boldsymbol{\tau}}{GM_\bullet}, \tag{2}$$

where $\boldsymbol{f}$ is the (specific) non-Keplerian gravitational force and $\boldsymbol{\tau} = {\rm d}\boldsymbol{j}/{\rm d}t$ is the specific orbit-averaged torque.

When a given stellar eccentricity vector is misaligned with the average eccentricity vector of the massive disc, it will experience

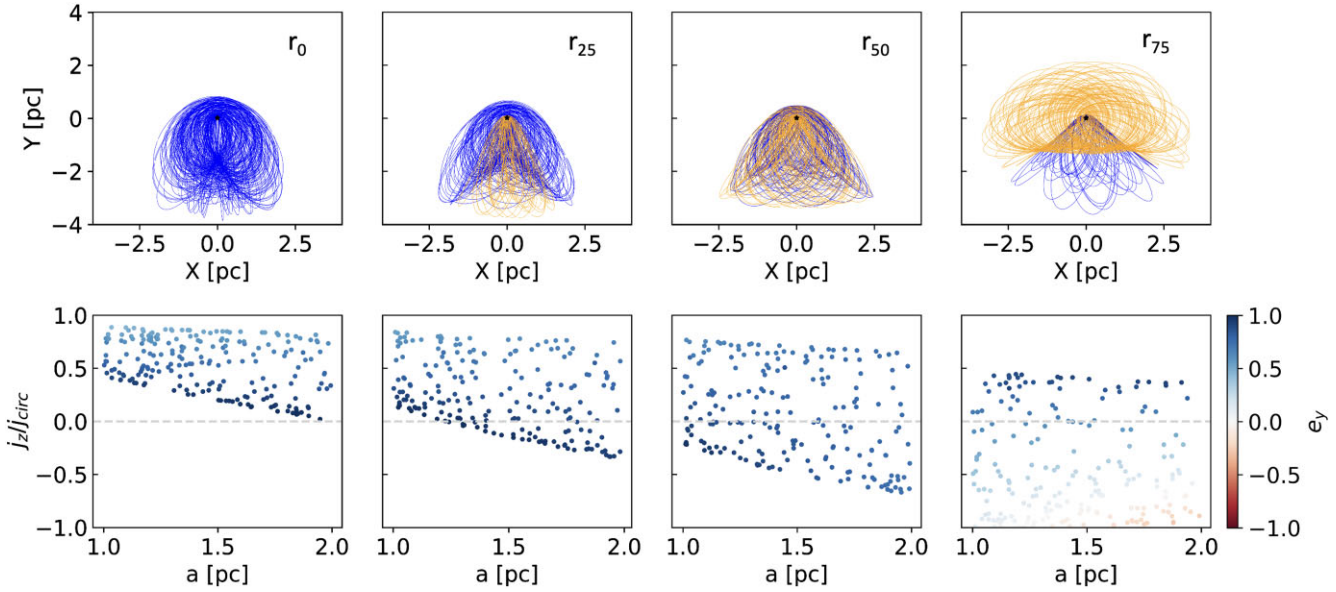

Figure 1. Initial post-kick stellar orbits in four sets of *N*-body simulations ($\boldsymbol{r_0}$,$\boldsymbol{r_{25}}$,$\boldsymbol{r_{50}}$, and $\boldsymbol{r_{75}}$). *Top*: Prograde (retrograde) orbits are in blue (orange). *Bottom*: z-component of the angular momentum of each star normalized by the circular angular momentum as a function of semimajor axis. The colour bar shows the y-component of the eccentricity vector.

a strong gravitational torque. If this torque is positive (relative to the orbit's angular momentum), it will serve to circularize the orbit, whereas if it is negative, it will serve to increase the orbit's eccentricity. In Fig. 2, we show the time evolution of the z-component of the angular momentum normalized by the circular angular momentum, $j_z/j_{\rm circ}$, of a single star in the r_{50} simulation. We also show $\Delta\theta$, the azimuthal angle between the star's eccentricity vector and the average eccentricity vector of the disc. The bottom panel shows a zoom-in of the shaded region in the top panel chosen for illustrative purposes to demonstrate the four possible states of the stellar orbit relative to the disc:

(A) When $j_z/j_{\rm circ} > 0$ (i.e. the star's angular momentum is prograde with respect to the disc) and $\Delta\theta > 0$ (i.e. the orbit has precessed ahead of the disc), the massive disc induces a negative torque on the star's orbit. This decreases the orbital angular momentum until $j_z/j_{\rm circ}$ passes through zero and the orbit flips to a retrograde orientation.

(B) When $j_z/j_{\rm circ} < 0$ (i.e. the star's orbit is retrograde), its precession is in the opposite direction, which acts to decrease $\Delta\theta$. The torque from the disc is now positive with respect to the stellar angular momentum, thereby decreasing its orbital eccentricity. The stellar orbit precesses past the bulk of the disc resulting in $\Delta\theta < 0$.

(C) When $j_z/j_{\rm circ} < 0$ and $\Delta\theta < 0$, the disc induces a negative torque on the star's angular momentum. This increases its orbital eccentricity and decreases $|j_z/j_{\rm circ}|$ until it flips orientation to become prograde. This is the inverse of (A).

(D) When $j_z/j_{\rm circ} > 0$, its precession is in the prograde direction, bringing it into alignment with the bulk of the disc and decreasing $|\Delta\theta|$. The bulk of the disc induces a positive torque on the star's orbit. This decreases the orbital eccentricity and increases $j_z/j_{\rm circ}$. This is the inverse of (B).

Orbit-averaged torques from the massive disc cause stellar orbits to oscillate continuously in angular momentum, flipping between prograde and retrograde (see top panel of Fig. 2). These oscillations contain the disc orbits in tight apsidal alignment (Section 4.2) and result in extreme TDE rates (Section 4.4). This torquing mechanism

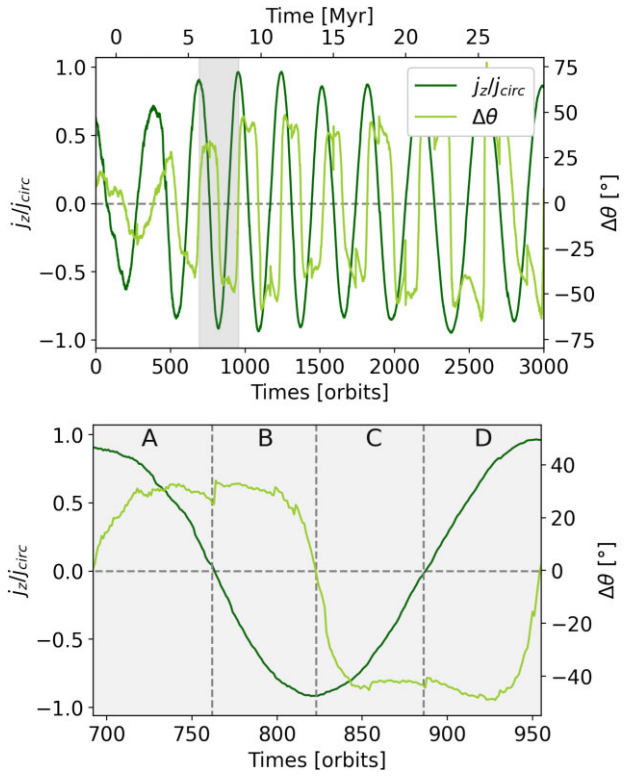

Figure 2. Flips in orbit orientation. *Top*: Time evolution of the z-component of the angular momentum, normalized to the circular angular momentum, for a sample star from the r_{50} model, and $\Delta\theta$ defined to be the azimuthal angle between the star's eccentricity vector and the average eccentricity vector of the disc. *Bottom*: A zoom-in of the shaded region of the top figure to illustrate the four different possibilities of the sample star's configuration relative to the bulk of the disc.

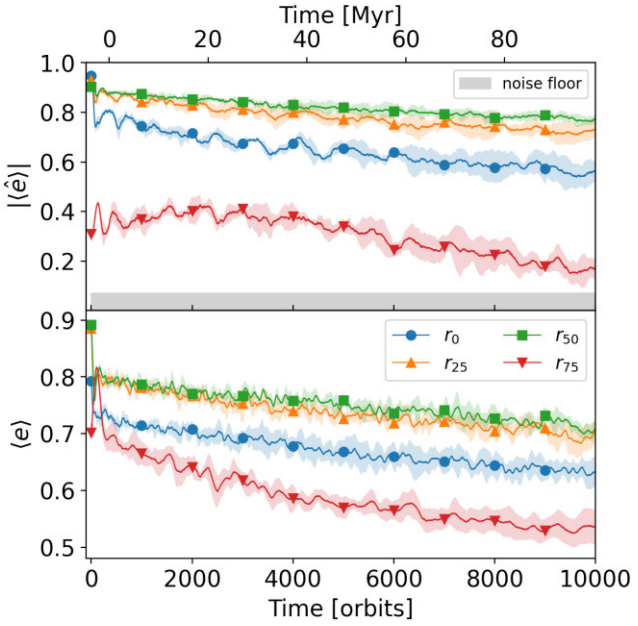

Figure 3. Disc alignment and average eccentricity evolution. *Top*: Time evolution of the average unit eccentricity vector of stars in the disc. Different coloured lines with symbols correspond to models of varying retrograde fraction. The noise floor, calculated as $1/\sqrt{N_{\rm bound}(t=0)}$, is shown with a grey shaded region. *Bottom*: Time evolution of the average eccentricity of all the stars in the disc.

is strongest in our r_{50} simulations in which the initial post-kick discs are apsidally aligned and the equal-mass prograde and retrograde populations begin to precess in opposite directions. Strong inter-orbit torques between the two oppositely precessing populations cause both populations to flip orientation and precess back towards each other. These dynamics repeat continuously.

4.2 Disc alignment and eccentricity evolution

We quantify the apsidal alignment of the disc using the average unit eccentricity vector

$$\langle \hat{e} \rangle = \frac{\sum_{i=1}^{N_{\rm bound}} \hat{e}_i}{N_{\rm bound}}, \tag{3}$$

where $\langle \hat{e} \rangle = 1$ indicates maximum apsidal alignment. The top panel of Fig. 3 shows the time evolution of the unit eccentricity vector for each of our simulations, showing the average (solid line) and standard deviation (shaded region) of the five realizations of each simulation set. Alignment is greatest for our r_{50} and r_{25} models, and lowest for our r_{75} model. The r_{75} model has the lowest alignment because it starts with a misalignment between the prograde and retrograde orbits (see Fig. 1).

We show the average orbital eccentricity as a function of time in the bottom panel of Fig. 3. All our simulations start with a large average eccentricity due to the impact of the recoil kick (pre-kick eccentricities are zero). Eccentricities remain very high when there is a significant retrograde fraction within the disc, with the largest values again in the r_{50} and r_{25} models. This is due to the strong negative torques (relative to the orbital angular momentum) between the two massive counter-rotating populations that drive a rapid decrease in the absolute value of angular momentum of each population, driving orbits to high eccentricities. While the r_{50} and r_{25} models have very similar average eccentricities, the distribution

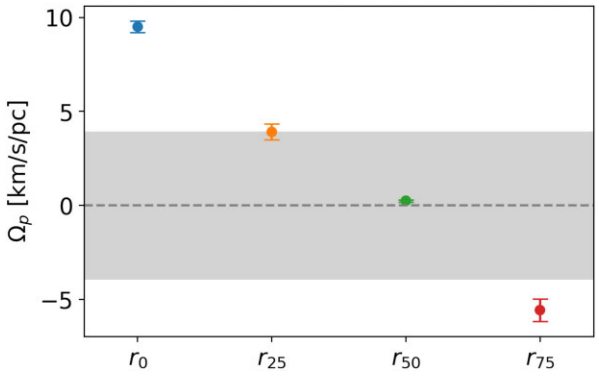

Figure 4. Precession rates as a function of retrograde fraction. The dashed line and shaded region indicate the range of precession rates that are consistent with the M31 eccentric nuclear disc (Lockhart et al. 2018).

of those eccentricities is different. In the r_{50} models, the prograde and retrograde populations have the same average eccentricity, while in the r_{25} models, the retrograde population has a higher average eccentricity. This is initially due to the orbital distribution caused by the recoil kick: in the r_{25} model, the only orbits that are flipped on to retrograde orbits are also highly eccentric, whereas in the r_{50}, more orbits are flipped on to retrograde orbits and have a wider range of eccentricities due to the fact that $v_{\rm kick}$ is greater and therefore there are more orbits for which $v_{\rm circ} \ll v_{\rm kick}$, so there can be retrograde orbits with lower eccentricities (see Fig. 1).

We note that the retrograde fraction at the end of our simulations is $(r_0, r_{25}, r_{50}, r_{75} = 0.17, 0.34, 0.47, 0.82)$. The r_0 and r_{25} simulations increase in retrograde fraction due to the fact that the inter-orbit torques cause some orbits to flip orientation, and this initially occurs primarily to the prograde population as it makes up the majority (or in the case of r_0, the entirety) of the disc (see also Rantala & Naab 2024). The retrograde fraction in the r_{25} simulation increases while it slightly decreases for the r_{50} simulation, accounting for their similar evolution.

The r_{75} simulation displays a qualitatively different behaviour. Due to the larger kick magnitude, the r_{75} starts with eccentricity vectors pointed in many different directions (see Fig. 1), and therefore there is initially a much lower amount of apsidal alignment in the disc (see Fig. 3). Inter-orbit torques are correspondingly weaker and less coherent. The prograde orbits are initially much more eccentric on average than the retrograde orbits (see Fig. 1), leading more of them to flip due to the inter-orbit torques and cause an increase in the retrograde fraction. Due to the initial apsidal spread of the orbits, the torques fail to align the orbits, and the average unit eccentricity vector, $\langle \hat{e} \rangle$, drops with time due to the differential precession.

4.3 Precession rate

We define the precession rate of the disc, $\Omega_{\rm P}$, as the time it takes the average eccentricity vector of the disc to complete a full 2π rotation. We take the average and standard deviation over the five realizations of each simulation set. To compare with the M31 nucleus, we augment the disc mass by a factor of 10. This augmentation is performed in post-processing due to computational limitations. The M31 eccentric disc is approximately an order of magnitude larger in both radial extent and mass, so this extrapolation is necessary to make meaningful comparisons with observed precession rates. The precession rates for each of our simulations can be seen in Fig. 4.

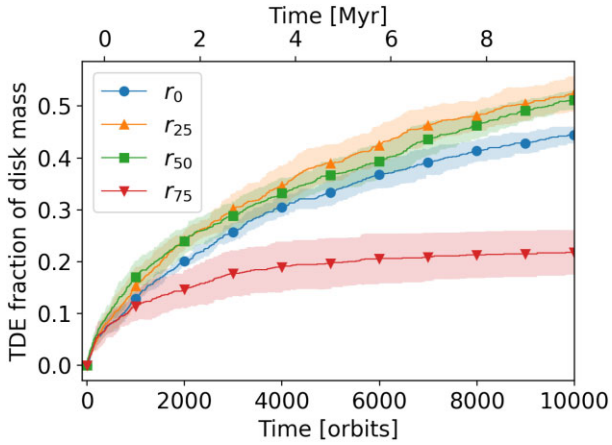

Figure 5. Fraction of the disc that has experienced a TDE as a function of time.

The range of values for the precession rate of the eccentric nuclear disc in M31 is shown as a grey shaded region (Lockhart et al. 2018).

In our r_{50} models, the precession rate of the aligned disc is nearly zero, in excellent agreement with Lockhart et al. (2018). The closer the retrograde fraction is to 50 per cent, the slower the precession rate. In simulations with more of one orientation, there is a net precession of the aligned disc in the direction dictated by the majority population. The precession rates for each of our simulations can be seen in Fig. 4. Our work provides a new mechanism to explain the slow precession rate in the M31 eccentric nuclear disc: a significant retrograde fraction caused by a recoil kick serves to keep the disc static, as well as maximally aligned.

4.4 Tidal disruption events

TDEs occur when a star passes within the tidal disruption radius of the black hole given by $R_{\rm T} = R_*(M_\bullet/M_*)^{1/3}$ (Rees 1988). Since the closest approach of a star is given by the periapsis distance $R_{\rm p} = a(1-e)$, large eccentricities result in significantly closer encounters with the black hole and increase the likelihood of disruption. TDE rates have been shown to be greatly enhanced in eccentric nuclear discs due to gravitational torques from the aligned disc driving oscillations in eccentricity (Madigan et al. 2018; Wernke & Madigan 2019, 2021).

Here, we explore the TDE rate in our four simulation sets. The supermassive black hole in M31 is too massive to produce observable TDEs, as its Schwarzchild radius is larger than the tidal disruption radius. We therefore scale our black hole mass to 10^7 $M_\odot$, $a_{\rm in} = 0.1$ pc, and we scale the stellar masses and radii to those of the Sun in order to calculate the tidal disruption radius.

We show our results in Fig. 5, plotting the fraction of stars in the disc that undergo a TDE as a function of time. We find a high TDE rate in all of our simulations that maintain high apsidal alignment. This is due to both the high average eccentricity in these simulations and the periodic gravitational torques that cause angular momentum values to pass through zero as orbit orientations flip. We see significantly lower TDE rates in the r_{75} simulation as this disc does not maintain high apsidal alignment or large eccentricities. Sufficiently high rates of TDEs will not appear as distinct events but rather have disrupting stars interacting with pre-existing TDE accretion discs. The build-up of numerous such discs may mimic the appearance of an active galactic nucleus, providing an electromagnetic counterpart to the GW signal of the black hole merger. We note that in these simple numerical experiments, we do not remove stars from our simulations after they experience a TDE, but simply count the first time that a star passes within the black hole tidal disruption radius. In reality, TDEs will remove mass but little angular momentum from the stellar disc, causing it to gain angular momentum per unit mass. Unless the disc mass can be replenished from the surrounding stellar potential, this will have two effects. One is to slowly circularize the eccentric nuclear disc and the other is to decrease the TDE rate over time.

5 DISCUSSION

We perform *N*-body simulations to investigate the long-term evolution of eccentric stellar nuclear discs around supermassive black holes formed due to GW recoil kicks. We simulate discs with both prograde and retrograde orbits, varying the magnitude of the recoil kick and thus the fraction of retrograde orbits within the disc. We describe the mechanism by which retrograde orbits help to maintain the disc's apsidal alignment through orbit-averaged torques between oppositely precessing prograde and retrograde populations. Our main findings are as follows:

(i) GW recoil kicks can produce any distribution of retrograde fraction in the orbits of a disc given different kick magnitudes, or initial stellar configurations. This is a new mechanism by which counter-rotation may be introduced into a galactic nucleus.

(ii) Large retrograde fractions are induced by large (relative to the pre-kick stellar orbital velocities) GW recoil kick velocities.

(iii) Aligned discs with a significant fraction of retrograde orbits are the most dynamically stable (Fig. 3).

(iv) Aligned discs with a significant fraction of retrograde orbits are the most eccentric (Fig. 3).

(v) Aligned discs with an equal fraction of prograde and retrograde orbits have near-zero precession rates (Fig. 4), consistent with that of M31's eccentric nuclear stellar disc (Lockhart et al. 2018).

(vi) Tidal disruption rates are greatly enhanced in eccentric nuclear discs with high apsidal alignment (Fig. 5).

GW recoil kicks spontaneously generate counter-rotating orbits in nuclear star clusters. This is an interesting new explanation for nuclei with significant counter-rotation (e.g. Gültekin et al. 2014). If this is the reason behind the near-zero precession rate of the M31 nuclear disc, our work also predicts that this disc contains a significant fraction of stars and stellar remnants on retrograde orbits. Sambhus & Sridhar (2002) find that a small fraction of retrograde orbits in their discs improves the fits to the observed kinematics and photometry of the M31 nucleus. We do not make a similar comparison here as we are simulating a narrow range in semimajor axes. In future, we will explore the impact of GW recoil kicks on the dynamics of realistic pre-kick stellar distributions scoured by merging supermassive black holes (Mastrobuono-Battisti et al. 2023) across a wider range of semimajor axes.

ACKNOWLEDGEMENTS

We gratefully acknowledge support from the David and Lucile Packard Foundation and National Science Foundation Graduate Research Fellowship grant DGE-1746060.

DATA AVAILABILITY

The data underlying this letter will be shared on reasonable request to the corresponding author.

REFERENCES

Akiba T., Madigan A.-M., 2021, ApJ, 921, L12
Akiba T., Madigan A.-M., 2023, ApJ, 958, 137
Bacon R., Emsellem E., Combes F., Copin Y., Monnet G., Martin P., 2001, A&A, 371, 409
Bekenstein J. D., 1973, ApJ, 183, 657
Bender R. et al., 2005, ApJ, 631, 280
Blanchet L., Qusailah M. S. S., Will C. M., 2005, ApJ, 635, 508
Bogdanović T., Reynolds C. S., Miller M. C., 2007, ApJ, 661, L147
Brown T. M., Ferguson H. C., Stanford S. A., Deharveng J.-M., 1998, ApJ, 504, 113
Campanelli M., Lousto C. O., Zlochower Y., Merritt D., 2007, Phys. Rev. Lett., 98, 231102
Chang P., Murray-Clay R., Chiang E., Quataert E., 2007, ApJ, 668, 236
Damour T., Gopakumar A., 2006, Phys. Rev. D, 73, 124006
Favata M., Hughes S. A., Holz D. E., 2004, ApJ, 607, L5
Generozov A., Nayakshin S., Madigan A. M., 2022, MNRAS, 512, 4100
Goodman J., 2003, MNRAS, 339, 937
Gültekin K., Gebhardt K., Kormendy J., Lauer T. R., Bender R., Tremaine S., Richstone D. O., 2014, ApJ, 781, 112
Herrmann F., Hinder I., Shoemaker D., Laguna P., Matzner R. A., 2007, ApJ, 661, 430
Hopkins P. F., Quataert E., 2010, MNRAS, 405, L41
Jacobs V., Sellwood J. A., 2001, ApJ, 555, L25
Kazandjian M. V., Touma J. R., 2013, MNRAS, 430, 2732
Kormendy J., Bender R., 1999, ApJ, 522, 772
Lauer T. R. et al., 1993, AJ, 106, 1436
Lauer T. R., Faber S. M., Ajhar E. A., Grillmair C. J., Scowen P. A., 1998, AJ, 116, 2263
Lauer T. R., Bender R., Kormendy J., Rosenfield P., Green R. F., 2012, ApJ, 745, 121
Light E. S., Danielson R. E., Schwarzschild M., 1974, ApJ, 194, 257
Lockhart K. E., Lu J. R., Peiris H. V., Rich R. M., Bouchez A., Ghez A. M., 2018, ApJ, 854, 121
McConnachie A. W., Irwin M. J., Ferguson A. M. N., Ibata R. A., Lewis G. F., Tanvir N., 2005, MNRAS, 356, 979
Madigan A.-M., Halle A., Moody M., McCourt M., Nixon C., Wernke H., 2018, ApJ, 853, 141
Mastrobuono-Battisti A., Ogiya G., Hahn O., Schultheis M., 2023, MNRAS, 521, 6089
Naoz S., 2016, ARA&A, 54, 441
Paczynski B., 1978, Acta Astron., 28, 91
Peiris H. V., Tremaine S., 2003, ApJ, 599, 237
Peres A., 1962, Phys. Rev., 128, 2471
Rantala A., Naab T., 2024, MNRAS, 527, 11458
Rauch K. P., Tremaine S., 1996, New Astron., 1, 149
Rees M. J., 1988, Nature, 333, 523
Rein H., Liu S. F., 2012, A&A, 537, A128
Rein H., Spiegel D. S., 2015, MNRAS, 446, 1424
Salow R. M., Statler T. S., 2001, ApJ, 551, L49
Salow R. M., Statler T. S., 2004, ApJ, 611, 245
Sambhus N., Sridhar S., 2002, A&A, 388, 766
Sridhar S., Saini T. D., 2010, MNRAS, 404, 527
Statler T. S., King I. R., Crane P., Jedrzejewski R. I., 1999, AJ, 117, 894
Touma J. R., 2002, MNRAS, 333, 583
Touma J. R., Sridhar S., 2012, MNRAS, 423, 2083
Touma J., Tremaine S., 2014, J. Phys. A: Math. Gen., 47, 292001
Touma J. R., Tremaine S., Kazandjian M. V., 2009, MNRAS, 394, 1085
Tremaine S., 1995, AJ, 110, 628
Wernke H. N., Madigan A.-M., 2019, ApJ, 880, 42
Wernke H. N., Madigan A.-M., 2021, ApJ, 920, 149
Wiseman A. G., 1992, Phys. Rev. D, 46, 1517

This paper has been typeset from a TEX/LATEX file prepared by the author.